Available online at www.sciencedirect.com
ScienceDirect
Journal of Power Sources 169 (2007) 315–326
JOURNAL OF POWER SOURCES
www.elsevier.com/locate/jpowsour

The influence of current collection on the performance of tubular anode-supported SOFC cells

Huayang Zhu *, Robert J. Kee

Engineering Division, Colorado School of Mines, Golden, CO 80401, USA

Received 19 February 2007; received in revised form 15 March 2007; accepted 16 March 2007
Available online 30 March 2007

Abstract

A mathematical model is developed and used to investigate the effects of axially distributed current collection on the performance of an anode-supported tubular solid oxide fuel cell (SOFC). The physical model considers coupled fluid and thermal transport within the tube, reactive porous-media flow within the electrodes, electrochemical charge-transfer, thermal transport within the MEA structure, and an electric circuit to represent the current-collection system. Four examples are used to illustrate the model and evaluate current-collection strategies. All the examples consider a particular Ni–YSZ | YSZ | LSM–YSZ tube, but with different current collection. The inlet fuel stream is a syngas mixture that results from steam reforming of dodecane. Results show that current collection can strongly affect local performance (i.e., composition, temperature, and current density profiles) along the length of the tube as well as overall performance (i.e., efficiency and utilization).

Keywords: SOFC; Tubular cell; Current collection; Modeling

1. Introduction

Tubular cells and stacks have some advantages compared to planar cells and stacks. For example, ceramic-to-metal seals are usually confined to small areas at the ends of the tubes. Fuel- and air-distribution manifolds may be more straightforward in tubular stacks. Stresses caused by thermal cycling can be less troublesome in tubular systems because the membrane-electrode assembly (MEA) is less rigidly confined. However, current collection is much more challenging in a tubular cell, especially for anode current collection on the inside of the tube. This paper develops a physically based computational model that can be used to evaluate alternative current-collection strategies.

Fig. 1 illustrates the nominal geometry for a tubular cell. This paper considers a porous cermet anode-supported tube, with the thin dense electrolyte and porous cathode applied to the outside of the tube. A typical tube wall may be fabricated as Ni–YSZ that is on the order of a millimeter thick. The dense electrolyte membrane is typically on the order of 10–20 μm of YSZ. A typical cathode may be 50 μm of porous LSM–YSZ. As illustrated in Fig. 1, the current collection is achieved by metallic wires that are bonded to the electrode surfaces. Additionally, a low-electrical-resistance bus is assumed to run axially the length of the tube.

In principle, because the electrodes have electrical conductivity, current could be collected axially through the electrode structures without any explicit current-collection structure. However, using typical electrode materials, the voltage drop would be far too high to be practical. The cathode especially is very thin and uses ceramic mixed ionic–electronic conducting (MIEC) materials that are relatively poor electronic conductors. The Ni in an Ni–YSZ has high electronic conductivity and the structure is relatively thick. Nevertheless, a dedicated low-resistance current-collection significantly improves performance.

The model in this paper considers fluid flow and heat-transfer within the tube, transport and catalytic chemistry within the porous electrodes, electrochemical charge-transfer, and heat-transfer within the MEA structure. An electrical network describes the current-collection system. Circumferential current-collection wires are attached to the electrodes at specified positions along the length of the tube. Usually, because of higher electrical-resistance in thin MIEC cathode materials, the cathode attachment is more frequent than the anode attachment.

* Corresponding author. Tel.: +1 303 273 3890; fax: +1 303 273 3602.
E-mail address: hzhu@mines.edu (H. Zhu).

0378-7753/$ – see front matter © 2007 Elsevier B.V. All rights reserved.
doi:10.1016/j.jpowsour.2007.03.047

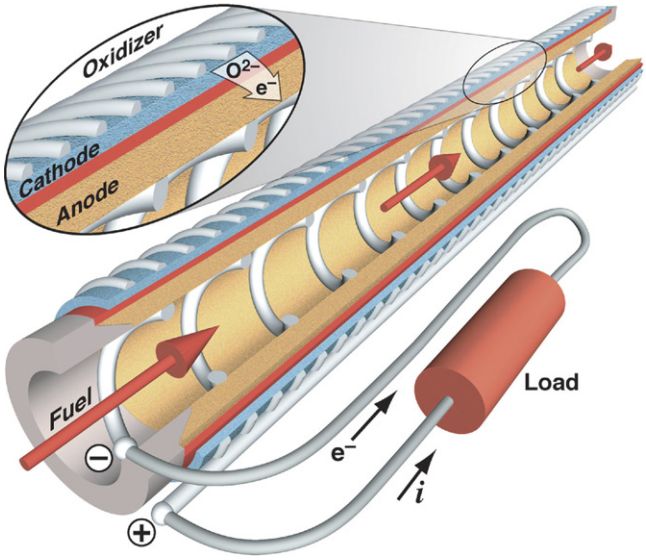

Fig. 1. Sketch of an anode-supported tubular SOFC.

An electrical-resistance is assigned to each attachment point, which may represent interface or bonding resistance. The attachment resistance may also account for the resistance to circumferential current flow in the wires leading to an axial bus. Each segment of the axial bus, between attachment points of the circumferential wires, is also assigned a resistance. The electrodes also have electrical-resistance. The model accounts for the local electric-potential profiles within the electrodes.

There is recent literature concerning the fabrication and performance of tubular cells [1–4]. These works are concerned primarily with ceramics materials processing. A number of recent modeling studies have also been developed to investigate the performance of tubular cell and systems [5–15].

Nagata et al. [5] and Aguiar et al. [6,7] solve energy and mass balances to represent one-dimensional steady-state reacting-flow for single-cell tubular SOFCs. Other groups have developed two-dimensional axisymmetric models [8–15]. These models predict pressure, temperature and species concentration distributions. In some cases circumferential current flow results in loss of full axisymmetry. Nevertheless, chemistry and heat release are based on circumferentially averaged electric potentials.

Charge-transfer chemistry is usually represented in Butler–Volmer form. Li et al. [8–11] assume that H_2 is the only electrochemically active species. They also assume that CH_4 reforming and water-gas-shift reactions are in equilibrium. Suwanwarangkul et al. [14] assume that H_2 and CO can both be electrochemically oxidized at the anode–electrolyte interface. They use a global rate expression for the water-gas-shift reaction. Nishino et al. [15] also considered that both H_2 and CO are electrochemically active. They represent CH_4 steam reforming and water-gas-shift reactions by the global kinetics. Campanari and Iora [12] assume that hydrogen is the only electrochemical active species. They use a global kinetic expression for CH_4 steam reforming and assume that the water-gas-shift reaction remains equilibrated.

Boersma et al. [16] develop an electric-network model for a single-tube fuel cells to describe the axial electric-potential distribution. The model incorporates ohmic losses across the MEA and along the length of the tube. For the particular system studied, the model predicts that the active tube length should be no longer than 10 cm due to the ohmic losses along the tube length, and the electrolyte should be less than 20 μm thick to achieve high power density. Suzuki et al. [17,18] have compared the current-collection efficiency for micro-tubular SOFCs, using either single-terminal or double-terminal anode current collection. They report that double-terminal anode current collector is much more efficient than single-terminal current collector.

The present paper considers the coupled effects of the current collection on fluid flow and chemistry, electric-potential distribution, and thermal behavior of the MEA structure and gas flow. The current-collection system, which directly affects the local cell potential, has an important impact on the overall cell performance. Thus, the current-collection system is an important aspect of tubular cell design and predictive models can greatly assist this process.

2. Mathematical models

The mathematical model in this paper builds on the model developed by Zhu et al. for planar cells [19]. In addition to considering a tubular geometry, the present model predicts the thermal response of the flow and the tube wall. The present model also incorporates the electrical behavior within the MEA and the current-collection system. The internal reforming chemistry and the charge-transfer models are the same as those in Zhu et al. [19].

2.1. Flow within the tube

The gas-phase flow in the tube is treated as a one-dimensional laminar flow, neglecting the spatial variations in the radial direction [20]. For syngas or methane fuels, homogeneous chemical kinetics are negligible for temperatures below around 900 ° C [21]. Using a plug-flow approximation, the mass and momentum conservation equations are summarized as

$$\frac{\partial \rho}{\partial t} + \frac{\partial \rho u}{\partial x} = -\frac{P_h}{A_c}\sum_{k=1}^{K_g} J_k^M W_k. \tag{1}$$

$$\frac{\partial(\rho u)}{\partial t} + \frac{\partial(\rho u^2)}{\partial x} = -\frac{\partial p}{\partial x} - \frac{P_h}{A_c}\tau_w, \tag{2}$$

$$\frac{\partial(\rho Y_k)}{\partial t} + \frac{\partial(\rho Y_k u)}{\partial x} + \frac{\partial j_k}{\partial x} = -\frac{P_h}{A_c} J_k^M W_k. \tag{3}$$

These equations are written in transient form, with the time t and the axial coordinate x being the independent variables. Dependent variables include the mass density ρ, the mean velocity u, the pressure p, and the species mass fractions Y_k. Geometric parameters include the hydrodynamic perimeter P_h and the cross-sectional flow area A_c. Assuming an inner tube diameter D, $P_h = \pi D$ and $A_c = \pi D^2/4$.

The density is determined from the pressure and composition using an ideal-gas equation of state

$$\rho = \frac{p\bar{W}}{RT} = \frac{p}{RT\sum_{k=1}^{K_g} Y_k/W_k}, \tag{4}$$

where R is the universal gas constant, T the temperature, $\bar{W}$ the mean molecular weight, and W_k are the species molecular weights. K_g is number of gas-phase species.

As a result of internal reforming and charge-transfer chemistry, there are species fluxes between the porous-anode structure and the flow within the tube. These molar fluxes are represented as J_k^M. As discussed in the following section, these fluxes are determined from the solution of the radial reactive porous-media problem within the MEA.

In addition to axial convective transport, there may be axial diffusion of species along the length of the tube. The axial diffusive mass fluxes are represented as

$$j_k = -\rho\frac{W_k}{\bar{W}}D_{km}\frac{\partial X_k}{\partial x}. \tag{5}$$

The mixture-average diffusion coefficients are calculated as,

$$D_{km} = \frac{1-Y_k}{\sum_{\ell\neq k}^{K_g} X_\ell/D_{k\ell}} \tag{6}$$

where X_k are the mole fractions, and $D_{k\ell}$ are the binary diffusion coefficients [20].

The wall shear stress τ_w is represented in terms of a friction factor $f = 2\tau_w/\rho u^2$. For a circular channel, the friction factor can be calculated based on the laminar, fully-developed flows as $Re\, f = 16$. The local Reynolds number is defined in terms of the mean velocity u and the hydraulic diameter as $Re = \rho u D/\mu$ where μ is the mixture viscosity.

2.2. Porous-electrode model

Because the electrodes are relatively thin and the axial gradients are low, axial and azimuthal species transport may be neglected within the porous anode structure. Radial transport and chemistry can be represented in one-dimensional form with overall and species continuity equations as

$$\frac{\partial(\phi\rho Y_k)}{\partial t} + \frac{\partial j_k^M}{\partial r} = A_s\dot{s}_k W_k, \tag{7}$$

$$\frac{\partial(\phi\rho)}{\partial t} + \sum_{k=1}^{K_g}\frac{\partial j_k^M}{\partial r} = \sum_{k=1}^{K_g} A_s\dot{s}_k W_k. \tag{8}$$

In these equations time t and radius r are the independent variables. The electrode porosity is ϕ and A_s is the specific surface area of the active catalysts (i.e., active surface area per unit volume of the porous media). The molar species production rates by heterogeneous reaction are represented as $\dot{s}_k$.

The gas-phase species mass fluxes j_k^M through the pore structure are determined from the Dusty-Gas Model (DGM) [22,19], which can be written as an implicit relationship among the gas-phase species molar fluxes J_k^M, molar concentration $[X_k]$, concentrations gradients, and the pressure gradient as,

$$\sum_{\ell\neq k}\frac{[X_\ell]J_k^M - [X_k]J_\ell^M}{[X_T]D_{k\ell}^e} + \frac{J_k^M}{D_{k,Kn}^e} = -\frac{\partial[X_k]}{\partial r} - \frac{[X_k]}{D_{k,Kn}^e}\frac{B}{\mu}\frac{\partial p}{\partial r}. \tag{9}$$

where $[X_T] = p/RT$ is the total molar concentration, B the permeability, and μ is the mixture viscosity. The radial mass fluxes are related simply to the molar fluxes as $j_k^M = W_k J_k^M$. The effective binary and Knudsen diffusion coefficients $D_{k\ell}^e$ and $D_{k,Kn}^e$ are written as

$$D_{k\ell}^e = \frac{\phi}{\tau}D_{k\ell}, \qquad D_{k,Kn}^e = \frac{4}{3}\frac{r_p\phi}{\tau}\sqrt{\frac{8RT}{\pi W_k}}. \tag{10}$$

The binary diffusion coefficients $D_{k\ell}$ and the mixture viscosities μ are determined from kinetic theory [20]. Knudsen diffusion represents mass transport assisted by gas–solid collisions. The Knudsen diffusion coefficients depend on physical characteristics of the porous media, including porosity ϕ, average pore radius r_p, primary particle diameter d_p, and tortuosity τ. The permeability can be determined from the Kozeny–Carman relationship as

$$B = \frac{\phi^3 d_p^2}{72\tau(1-\phi)^2}. \tag{11}$$

Further details of the DGM and its numerical implementation can be found in Zhu et al. [19].

Heterogeneous chemical kinetics proceeds on the catalyst surfaces within the porous anode. Molar production rates by the heterogeneous reactions $\dot{s}_k$ are functions of temperature, gas concentrations, and surface-species coverages. The reaction mechanism used in the present model incorporates steam and dry reforming as well as partial oxidation [23]. This mechanism considers 42 reactions among 6 gas-phase species and 12 surface-adsorbed species. Temporal variations of the site coverages θ_k of the K_s surface-adsorbed species are represented as

$$\frac{d\theta_k}{dt} = \frac{\dot{s}_k}{\Gamma}, \quad k = 1,\ldots,K_s \tag{12}$$

where Γ is the available site density. At steady-state, $\dot{s}_k = 0$.

Boundary conditions are needed to solve Eqs. (7) and (8) within the porous electrodes. At the interfaces between the porous electrode and the external gas flow (i.e., fuel within the tube or air outside the tube) the gas-phase composition is assumed to be that within the either the fuel or air flow. At the electrode-electrolyte interfaces, species fluxes are established by the electrochemical charge-transfer reactions within thin electrode-electrolyte three-phase boundary (TPB) regions as

$$j_k^M = -\frac{W_k\nu_k}{n_e F}i_e, \tag{13}$$

where i_e is the local current density, F the Faraday's constant, ν_k the stoichiometric coefficients in a global charge-transfer reaction and n_e is the number of electrons transferred. For hydrogen oxidation at the anode–electrolyte interface (i.e., $H_2 + O^{2-} \rightleftarrows H_2O + 2e^-$), $\nu_{H_2} = -1$, $\nu_{H_2O} = 1$, and $n_e = 2$. For oxygen reduction at the cathode-electrolyte interface (i.e., $O_2 + 4e^- \rightleftarrows 2O^{2-}$), $\mu_{O_2} = 1$ and $n_e = 4$.

The gas-flow equations and the porous-media equations are intimately coupled. The species molar fluxes between the surface of the porous electrode and the adjoining gas flow (i.e., the J_k^M terms in Eqs. (1) and (3)) are evaluated from the porous-media solution at the interface. The gas-flow composition (determined from Eqs. (1) and (3)) serves as boundary conditions for the reactive porous-media problem (i.e., Eqs. (7) and (8)).

2.3. Electrochemistry

The operating cell potential between anode and cathode at the dense-electrolyte interfaces E_{cell} may be represented in terms of overpotentials as

$$E_{cell} = E_{rev} - \eta_{act,a}(i_e) - \eta_{ohm}(i_e) - |\eta_{act,c}(i_e)|, \tag{14}$$

where E_{rev} is the reversible potential across the dense electrolyte membrane (i.e., *not* the reversible potential based on the electrochemical potentials of the gases in the anode and cathode compartments). The reversible potential E_{rev}, the cell potential E_{cell}, and the current density i_e all vary continuously along the length of the tube. The activation overpotentials at the anode–electrolyte and cathode-electrolyte interfaces are written as $\eta_{act,a}$ and $\eta_{act,c}$, respectively. The ohmic overpotential is written as η_{ohm}. Because gas-phase transport and chemistry within the electrode structure are modeled fully in this formulation, there is no explicit need to incorporate a "concentration overpotential."

The current density is written in terms of the Butler–Volmer equation as

$$i_e = i_0 \left[\exp\left(\frac{\alpha_a F \eta_{act}}{RT} \right) - \exp\left(-\frac{\alpha_c F \eta_{act}}{RT} \right) \right], \tag{15}$$

where i_0 is the exchange current density, F is the Faraday constant, and α_a and α_c are the anodic and cathodic symmetry parameters.

The exchange current density at the anode is given as [19]

$$i_0 = i^*_{H_2} \frac{(p_{H_2}/p^*_{H_2})^{1/4} (p_{H_2O})^{3/4}}{1 + (p_{H_2}/p^*_{H_2})^{1/2}}. \tag{16}$$

The parameter $p^*_{H_2}$ depends on hydrogen adsorption/desorption rates. The dependence of the exchange current density i_0 on the temperature can be expressed as,

$$i^*_{H_2} = i^*_{ref,H_2} \exp\left[-\frac{E_{H_2}}{R} \left(\frac{1}{T} - \frac{1}{T_{ref}} \right) \right], \tag{17}$$

where E_{H_2} is the apparent activation energy for the electrochemical oxidation of H_2, and the parameter i^*_{ref,H_2} is assigned empirically to fit measured polarization data at a reference temperature T_{ref}. Similarly, at the cathode, the exchange current density is expressed as

$$i_0 = i^*_{O_2} \frac{(p_{O_2}/p^*_{O_2})^{1/4}}{1 + (p_{O_2}/p^*_{O_2})^{1/2}}, \tag{18}$$

where

$$i^*_{O_2} = i^*_{ref,O_2} \exp\left[-\frac{E_{O_2}}{R} \left(\frac{1}{T} - \frac{1}{T_{ref}} \right) \right]. \tag{19}$$

E_{O_2} is the apparent activation energy for the electrochemical reduction of O_2. The parameter $p^*_{O_2}$ depends on O_2 adsorption/desorption rates and the parameter i^*_{ref,O_2} is assigned empirically. All the partial pressures in Eqs. (16) and (18) are measured in atmospheres.

2.4. Tube flow energy balance

This model considers three temperatures: the gas temperature within the anode tube T_a, the tube-wall temperature T_m, and the external air temperature T_c. The thermal balance among the fuel-cell components includes convective heat-transfer between flow in the tube and the MEA structure, convective heat-transfer between the outside air and MEA structure, heat transport associated with species transport between the electrodes and the adjoining gas, and axial heat conduction within the tube wall. Source terms appear in the energy balance for the tube wall (i.e., the MEA) to describe heat release associated with thermal reactions within the porous electrodes, electrochemical charge-transfer reactions, and ohmic heat generation.

Energy conservation for gas flow within the tube can be expressed as

$$\frac{\partial E}{\partial t} + \frac{\partial q}{\partial x} = -\frac{P_h}{A_c}(q^T + q^M), \tag{20}$$

where $E = \rho e$ and e is the specific internal energy of the gas. The heat flux q, which represents both axial heat conduction and gas-phase species transport, is written as

$$q = -\lambda \frac{\partial T}{\partial x} + \sum_{k=1}^{K_g} (\rho Y_k u + j_k) h_k, \tag{21}$$

where h_k are the species specific enthalpies and λ is the mixture thermal conductivity.

The convective heat flux between the tube flow and the MEA structure is represented as

$$q^T = h_{conv}(T - T_m), \tag{22}$$

where h_{conv} is a convective heat-transfer coefficient. Within the tube, h_{conv} may be evaluated using a conventional Nusselt-number correlation.

The second term on the right-hand side of Eq. (20) (i.e., q^M) represents the energy transport associated with mass transfer between the channel flow and the porous anode structure (i.e., tube wall). Because all the heat release (i.e., resulting from thermal and electrochemical reactions and ohmic heat resistance) is assigned to the MEA structure, q^M must be subtracted from the

conservative form of the tube-flow energy equation (Eq. (20)). In the conservative form, the tube-flow energy equation implicitly contains the heat released in the porous electrode through the species continuity equations.

The heat flux associated with species transport between the MEA structure and the tube flow q_a^M can be written as

$$q_a^M = \sum_{J_k^M>0} J_k^M W_k h_k(T_a) + \sum_{J_k^M\le 0} J_k^M W_k h_k(T_m). \quad (23)$$

If species transfer from the tube into the MEA structure, enthalpies of the gas-phase species h_k are evaluated at the tube gas temperature T_a, otherwise, h_k are evaluated at the MEA temperature T_m. Note that $J_k^M > 0$ indicates radially outward flux. Heat flux between the outside of the tube (cathode) and the air can be written as

$$q_c^M = -\sum_{J_k^M<0} J_k^M W_k h_k(T_c) - \sum_{J_k^M\ge 0} J_k^M W_k h_k(T_m). \quad (24)$$

In this expression, J_k^M is the molar flux at the exterior surface of the cathode. In this case, $J_k^M > 0$ means gas is leaving the cathode and entering the surrounding air.

The heat-transfer coefficient within the tube h_{conv} can be evaluated based on a Nusselt-number correlation as,

$$Nu = \frac{h_{conv} D}{\lambda}. \quad (25)$$

For the laminar flow in a circular channel with constant wall temperature, the Nusselt number can be calculated as [24,25],

$$Nu = 3.657 + 6.874\left(\frac{1000}{Gz}\right)^{-0.488} \exp\left(-\frac{57.2}{Gz}\right), \quad (26)$$

where the Graetz number is defined as $Gz = Re\ Pr\ D/x$.

2.5. MEA energy balance

The MEA is assumed to have a uniform temperature radially, but varying axially. Further, the solid materials and the gas within the pore spaces are at a common temperature T_m. Energy conservation for the MEA structure may be written as

$$\frac{\partial E_m}{\partial t} + \frac{\partial q_m}{\partial x} = \dot{q}_{mea} + \frac{P_h}{A_m} q_a^T + \frac{P_o}{A_m} q_c^T, \quad (27)$$

where E_m is the total energy per unit volume of the MEA structure, P_o the outside perimeter of the tube and $A_m = \pi(r_o^2 - r_h^2)$ is the cross-sectional area of the tube wall. The net volumetric heat source within the MEA structure, due to the thermal and electrochemical reactions and the ohmic resistance, may be written as

$$\dot{q}_{mea} = \frac{P_h}{A_m} q_a^M + \frac{P_o}{A_m} q_c^M - \frac{P_e}{A_m} i_e E_{cell}. \quad (28)$$

In this equation P_e is the perimeter of the dense electrolyte. Axial conduction within the MEA structure is written as

$$q_m = -\lambda_m \frac{\partial T_m}{\partial x}, \quad (29)$$

where λ_m is the effective thermal conductivity of the composite MEA structure.

Eq. (27) is second order and requires boundary conditions at both ends of the tube. The results discussed later in this paper assume that the tube wall is insulated at both ends.

3. Electrical network

Electrons in the cathode participate in charge-transfer reactions to reduce the oxygen, and the electrons released by electrochemical fuel oxidation are delivered into the anode. The role of the current-collection architecture is to distribute electrons with minimal ohmic losses. Referring again to Fig. 1, we assume that the terminal voltage (i.e., cell potential) is fixed at one end of the tube. The current-collection system is formed by circumferentially wrapped high-conductivity wires that contact the electrodes and axial wires (buses) that carry current to the terminals. The electrode materials are also electrically conductive. However, it is presumed that the electrical conductivity within the electrodes (especially the cathode) is lower compared to the current-collection system.

The net electrical-resistance (i.e., electrodes and current collection) serves to increase the local operating potential $E_{cell}(x)$ along the length of the tube. This, in turn, limits the current that can be generated electrochemically. If the resistance is sufficiently great as to cause the local cell potential to reach the local open-circuit potential at some position x (i.e., $E_{cell}(x) = E_{rev}(x)$), the remainder of the cell cannot produce electric current. In addition to primarily electrical aspects, there are potentially important consequences on thermal behavior and overall cell efficiency. Thus, careful design of the current-collection system to reduce net electrical-resistance is a very important aspect of tubular SOFC design.

Fig. 2 illustrates an electric-circuit model that represents a single tubular SOFC cell. The cathode bus is represented as a series of resistances $R_{c,i}^B$. This bus is connected to the cathode itself via an array of attachments that have resistances $R_{c,i}^A$. There is also axial electrical conduction within the cathode structure, which is represented through its effective electrical conductivity σ_c^e. In this circuit, the dense electrolyte behaves as an axially distributed current source (much like a locally distributed battery). The anode side of the network is constructed in a way that is analogous to the cathode. Electrons flow from the porous anode structure through discrete attachment points into the anode bus, and ultimately to the cell terminal. As with the cathode, the anode structure has electrical conductivity σ_a^e, and the attachment and bus have resistances $R_{a,i}^A$ and $R_{a,i}^B$, respectively. Because the anode and the cathode materials may have very different electric conductivities, the number of attachments and the resistances of the interconnect bus may be very different for the anode and the cathode current collection.

The anode side of the electrical network may be represented with charge-conservation equations as

$$\frac{\partial}{\partial x}\left(\sigma_a^e \frac{\partial \Phi_a}{\partial x}\right) = i_e(x) + \sum_{i=1}^{n_a^A} \frac{\Phi_a(x_i) - \Phi_{a,i}^B}{R_{a,i}^A} \delta(x - x_i), \quad (30)$$

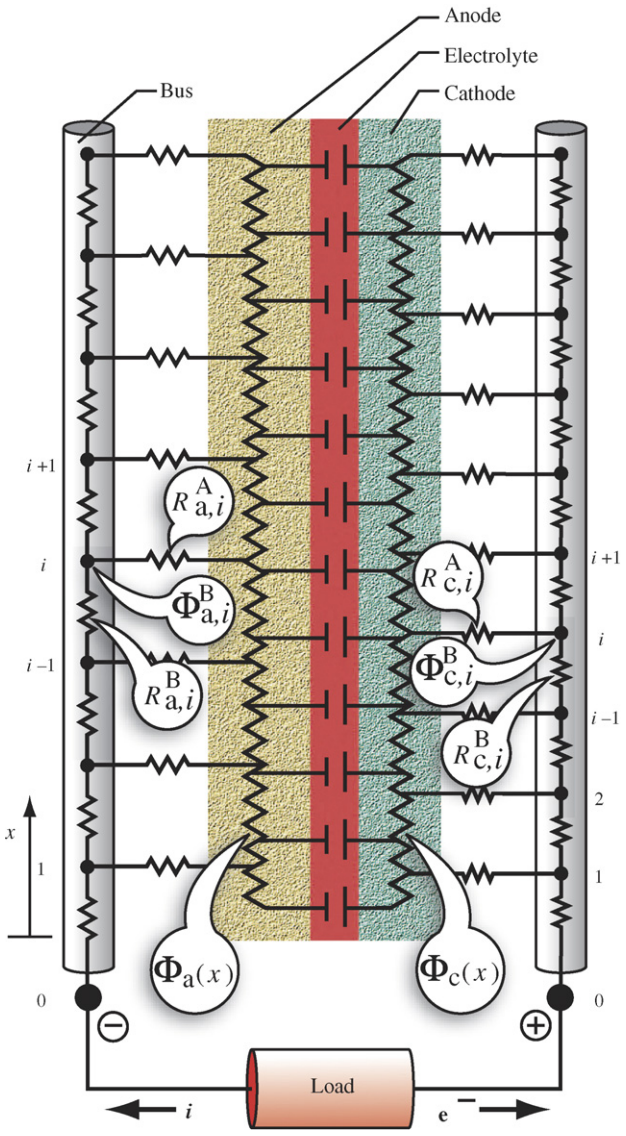

Fig. 2. Illustration of the electric circuit model for a single cell tubular SOFC.

$$\frac{\Phi^{\mathrm{B}}_{\mathrm{a},i} - \Phi^{\mathrm{B}}_{\mathrm{a},i-1}}{R^{\mathrm{B}}_{\mathrm{a},i}} + \frac{\Phi^{\mathrm{B}}_{\mathrm{a},i} - \Phi^{\mathrm{B}}_{\mathrm{a},i+1}}{R^{\mathrm{B}}_{\mathrm{a},i+1}} + \frac{\Phi^{\mathrm{B}}_{\mathrm{a},i} - \Phi_{\mathrm{a}}(x_i)}{R^{\mathrm{A}}_{\mathrm{a},i}} = 0. \tag{31}$$

In these equations, Φ_{a} is the anode electric potential and $\Phi^{\mathrm{B}}_{\mathrm{a},i}$ is the electric potential at the attachment node i of the anode interconnect bus. The Dirac delta function is δ, and $n^{\mathrm{A}}_{\mathrm{a}}$ is the number of attachments between the anode and the anode interconnect bus. Eq. (30) is a balance equation for the local electric potential $\Phi_{\mathrm{a}}(x)$ within the porous anode structure. The right-hand side has local source terms for the current production $i_{\mathrm{e}}(x)$ and the current provided from the bus through the $n^{\mathrm{A}}_{\mathrm{a}}$ discrete attachment points. Eq. (31) represents the charge-balance at each attachment point i. Without capacitance in the circuit, the net rate of charge accumulation at each node must vanish. This means that the sum of the currents at a node must vanish.

Charge balance on the cathode side of the network is represented as

$$\frac{\partial}{\partial x}\left(\sigma^{\mathrm{e}}_{\mathrm{c}}\frac{\partial \Phi_{\mathrm{c}}}{\partial x}\right) = -i_{\mathrm{e}}(x) + \sum_{i=1}^{n^{\mathrm{A}}_{\mathrm{c}}} \frac{\Phi_{\mathrm{c}}(x_i) - \Phi^{\mathrm{B}}_{\mathrm{c},i}}{R^{\mathrm{A}}_{\mathrm{c},i}}\delta(x - x_i), \tag{32}$$

$$\frac{\Phi^{\mathrm{B}}_{\mathrm{c},i} - \Phi^{\mathrm{B}}_{\mathrm{c},i-1}}{R^{\mathrm{B}}_{\mathrm{c},i}} + \frac{\Phi^{\mathrm{B}}_{\mathrm{c},i} - \Phi^{\mathrm{B}}_{\mathrm{c},i+1}}{R^{\mathrm{B}}_{\mathrm{c},i+1}} + \frac{\Phi^{\mathrm{B}}_{\mathrm{c},i} - \Phi_{\mathrm{c}}(x_i)}{R^{\mathrm{A}}_{\mathrm{c},i}} = 0. \tag{33}$$

In these equations, Φ_{c} is the cathode electric potential and $\Phi^{\mathrm{B}}_{\mathrm{c},i}$ is the electric potential at the attachment node i of the cathode interconnect bus.

The local electric-potential difference across the MEA structure can be calculated as the potential difference between the cathode and the anode as

$$E_{\mathrm{cell}}(x) = \Phi_{\mathrm{c}}(x) - \Phi_{\mathrm{a}}(x). \tag{34}$$

Assuming that the output operating cell voltage E_{out} is given, the terminal potential at the anode interconnect bus can be set to be zero as $\Phi^{\mathrm{B}}_{\mathrm{a},0} = 0$, and the terminal potential at the cathode interconnect bus can be set as the output operating cell potential as $\Phi^{\mathrm{B}}_{\mathrm{c},0} = E_{\mathrm{out}}$.

4. Numerical algorithm

The numerical solution of the coupled model is obtained by solving sequentially and iteratively three submodels: the fluid flow and heat transport along the channel length, the cell electric-potential distribution along the axial bus and the MEA structure, and the chemically and electrochemically reacting flows within the porous electrodes and electrolyte. At each iteration step, all the flow stream properties (i.e., gas composition Y_k, temperatures T_{a}, T_{c}, and T_{m}, and pressure p) and cell voltage E_{cell} are first frozen. A one-dimensional MEA model is solved to obtain the electric current i_{e} across the MEA structure, the heat fluxes $q^{\mathrm{M}}_{\mathrm{a}}$ and $q^{\mathrm{M}}_{\mathrm{c}}$, and the gas-phase species mass fluxes j^{M}_k between the flow streams and the electrodes. Then, by freezing the $q^{\mathrm{M}}_{\mathrm{a}}$, $q^{\mathrm{M}}_{\mathrm{c}}$, and j^{M}_k computed from the MEA model, the fluid flows and the temperatures along the channel are recalculated. The cell-voltage distribution along the channel is solved by freezing the current density i_{e} through the MEA structure.

Spatial derivatives in all the governing equations are discretized using the finite-volume method. The transient problem of the MEA submodel is solved using a method-of-lines algorithm, with the time marching accomplished with the LIMEX software that is designed to solve systems of differential-algebraic Eq. [26]. The steady-state problem for the channel flow and the temperature is solved as a boundary-value problem using a hybrid-Newton method [27,20].

5. Results and discussions

A particular anode-supported tube is used to illustrate the effects of the current-collection network on cell performance. The tube's inner diameter is $D = 0.8$ cm and it is $L = 25$ cm long. The anode is 900 μm of porous Ni–YSZ, the electrolyte is

Table 1
Physical and chemical parameters for the MEA structure

Parameters	Value
Anode	
Thickness, L_a (μm)	900
Porosity, ϕ	0.35
Tortuosity, τ	4.80
Pore radius, r_p (μm)	0.20
Particle diameter, d_p (μm)	1.00
Specific catalyst area, A_s (cm^{-1})	1080
Apparent activation energy, E_{H_2} ($kJ\,mol^{-1}$)	120.0
Reference temperature, T_{ref} (K)	1073.0
Exchange current factor, i^*_{ref,H_2} ($A\,cm^{-2}$)	8.5
Anodic symmetry factor, α_a	1.5
Cathodic symmetry factor, α_c	0.5
Cathode	
Thickness, L_c (μm)	50
Porosity, ϕ	0.35
Tortuosity, τ	4.00
Pore radius, r_p (μm)	0.25
Particle diameter, d_p (μm)	1.25
Apparent activation energy, E_{O_2} ($kJ\,mol^{-1}$)	130.0
Reference temperature, T_{ref} (K)	1073.0
Exchange current factor, i^*_{ref,O_2} ($A\,cm^{-2}$)	2.4
Anodic symmetry factor, α_a	1.5
Cathodic symmetry factor, α_c	0.5
Electrolyte: $\sigma_{el} = \sigma_0 T^{-1} \exp(-E_{el}/RT)$	
Thickness, L_{el} (μm)	20
Activation energy, E_{el} ($J\,mol^{-1}$)	8.0E4
Ion conductive pre-factor, σ_0 ($S\,cm^{-1}$)	3.6E5

20 μm YSZ, and the cathode is 50 μm of porous LSM–YSZ. Table 1 lists other parameters that describe the MEA structure. The apparent activation energies for the exchange current densities are taken from Nagata et al. [5]. The exchange-current-density factors i_{ref}, H_2^* and i^*_{ref,O_2} are estimated by fitting the experimental data at the reference temperature $T_{ref} = 1073$ K.

The thermal conductivities of the anode, cathoed and electrolyte are taken to be 11.0, 6.23, and 2.7 $W\,m^{-1}\,K^{-1}$, respectively [15]. The effective thermal conductivity of the MEA structure is estimated to be $\lambda_m = 10.5\,W\,m^{-1}\,K^{-1}$.

The effective anode and cathode electric conductivities ($S\,cm^{-1}$) can be evaluated as functions of temperature in the form [28]

$$\sigma^e = A^e T^{-1} \exp\left(-\frac{E^e}{RT}\right). \quad (35)$$

Values for the pre-factors A^e and activation energies E^e are listed in Table 2. Illustrative values of attachment and bus resistances also are shown in Table 2. The bus resistance R' is stated per unit length. Thus, the net bus resistance between attachment points is $R^B = R'L$. where L is the distance between attachments points. Assuming the buses are made of silver (electrical resistivity at 800 °C, $\rho_e = 6.5 \times 10^{-6}\,\Omega$ cm), the bus resistances in Table 2 correspond to bus diameters of 3.2 mm for the cathode and 4.5 mm for the anode.

In all cases the inlet fuel composition is 53.3% H_2, 24.6% H_2O, 12.3% CO, 9.2% CO_2, and 0.6% CH_4. This is the equilibrium output of a steam reformer operating on dodecane ($C_{12}H_{26}$) at 700 °C, 1 atm, and a steam-carbon ratio of 2.5. The tube inlet velocity is 60 $cm\,s^{-1}$ and the inlet temperature is 750 °C. The terminal voltage is fixed at $E_{out} = 0.65$ V. The model is developed to consider the air depletion by solving the air flow through the air channel. But the air compartment for all the examples presented here is assumed to be flooded by the air such that the variations of species composition and temperature along the channel are negligible. The external air temperature and pressure are fixed to be 750 ° C and 1 atm. The heat-transfer coefficient between the cathode and the external air is taken to be 100 $W\,m^{-2}\,K^{-1}$.

To explore the influence of current-collection strategies and to assist interpreting model results, four alternatives for current-collection systems are investigated. They are:

Base case: The base case uses 50 cathode-attachment points and 10 anode-attachment points.
Reduced cathode attachment: This case is the same as the base case, but with only 25 cathode attachment points.
Without anode collection: This case assumes that the cathode electric potential is uniform (i.e. perfect cathode current collection), and that all anode current collection is accomplished by axial conduction through the anode itself (i.e., no attachment points or anode bus).
Uniform cell potential: This case assumes perfect current collection, such that the the cell potential $E_{cell} = E_{out} = 0.65$ V everywhere along the tube.

Fig. 3 shows a composite of computed solutions for the base case. The local cell potential and current density show a sawtooth-like behavior, with the period set primarily by the cathode attachment points. The current (and power) density is nearly exactly out of phase with the cell potential. At the attachment points, where the cell potential is locally minimum, the current density is high. A low-frequency oscillation can also be seen, especially in the cell potential. This period is set by the less-frequent anode attachment.

The bottom panel of Fig. 3 shows temperature and velocity profiles. Because of heat release due to chemistry, electrochemistry, ohmic heat generation within the MEA, the tube-wall temperature increases in the entry regions where the current density is high. Relatively high thermal conductivity in the wall allows significant axial heat conduction. Fuel enters the tube at

Table 2
Electrical parameters for the MEA and current collection

Parameters	Value
Anode	
Conductivity pre-factor, A^e_a ($S\,K\,cm^{-1}$)	9.5×10^5
Conductivity activation energy, E^e_a ($J\,mol^{-1}$)	9561.1
Attachment resistance, R^A_a (Ω)	1×10^{-5}
Bus resistance, R'_a (Ω cm^{-1})	4×10^{-5}
Cathode	
Conductivity pre-factor, A^e_c ($S\,K\,cm^{-1}$)	4.2×10^5
Conductivity activation energy, E^e_c ($J\,mol^{-1}$)	9976.8
Attachment resistance, R^A_c (Ω)	1×10^{-5}
Bus resistance, R'_c (Ω cm^{-1})	8×10^{-5}

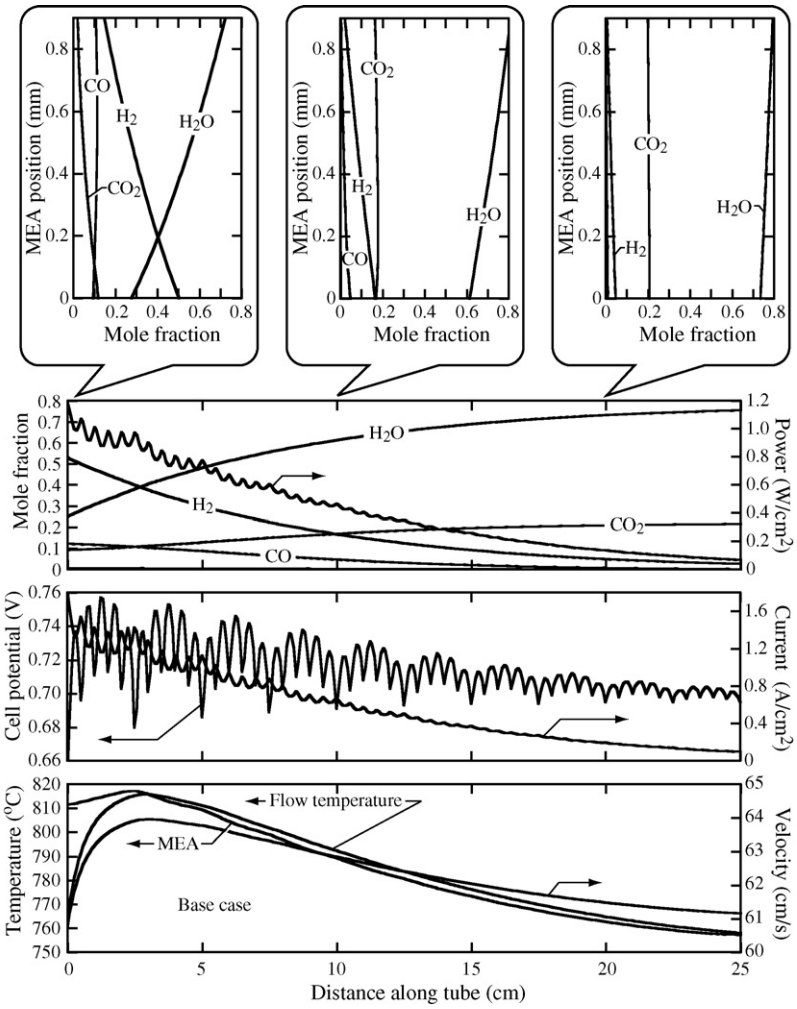

Fig. 3. Composite solution profiles for the base case.

750 ° C and is heated by convection from the wall. However, as the flow proceeds along the channel, fuel is depleted and current density decreases. This, in turn, reduces the heat generation within the wall. Also, the tube is losing heat convectively to the exterior relatively cool air at 750 °C. In the downstream sections of the tube, the flow carries energy from the upstream high-temperature regions downstream. In the downstream sections, the flow temperature slightly exceeds the tube-wall temperature. The velocity profile shows very little variation. This is because there is no molar change associated with oxidizing the syngas mixture. The shape of the velocity profile is caused primarily by the density variation associated with the temperature profile.

Species profiles along the tube length show expected behavior. Hydrogen levels decrease owing primarily to electrochemical oxidation. Carbon monoxide levels decrease owing primarily to water-gas-shift processes that react CO and steam to produce H_2 and CO_2. The product species, H_2O and CO_2 increase steadily along the length of the tube. The upper panels of Fig. 3 show gas-phase species profiles through the thickness of the porous anode at three locations along the tube. Again, expected behavior is observed. In the entry regions, strong gradients in hydrogen and steam are caused by charge-transfer reactions in the three-phase region near the dense electrolyte (top of the plots). Curvature in the profiles is caused by catalytic chemistry (primarily water-gas-shift) within the anode. In the downstream regions the gradients are diminished as the fuel is depleted and the current density is reduced.

Fig. 4 shows the electric-potential profiles within the anode, anode bus, cathode, and cathode bus along the tube length.

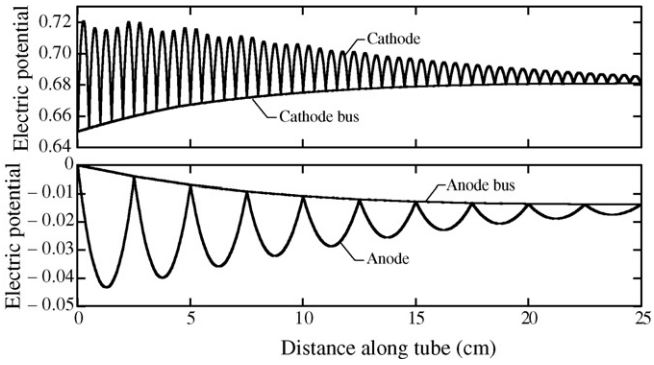

Fig. 4. Local electric-potential profiles for the base case.

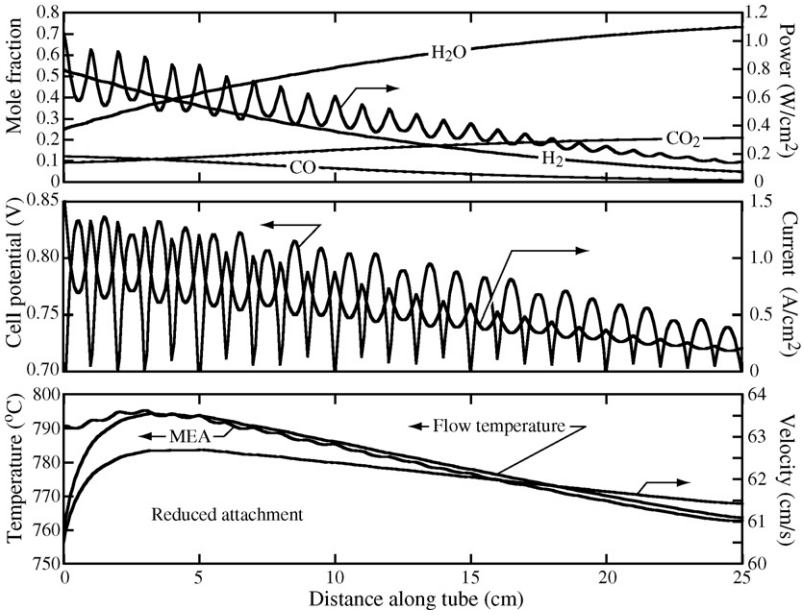

Fig. 5. Composite solution profiles for the reduced-attachment case.

The terminal potential (at $x = 0$) is fixed at 0.65 V. Because of relatively low resistance in the axial buses, the electric-potential profiles along the busses are smooth. Also, because the attachment resistances are low in this example, there is very little electric potential difference across the attachment points. Although the axial busses have relatively lower resistance than the electrodes, they still have resistance. Thus, the cell potential (difference between cathode and anode potentials) must increase along the tube length, driving current toward the terminals at the left-hand side of Fig. 4. The current collection in this example is reasonably effective, with a net variation of cell potential between the axial buses of only about 0.05 V.

It is evident from Fig. 4 that there can be significant electric-potential variation within the electrodes between the attachment points. Because of relatively high resistance within the electrodes, a potential difference is required to drive electric current axially along electrodes toward the attachment points. With the parameters in this example, local potential variations within the anode are about 0.015 V and within the cathode are about 0.03 V. Although the terminal potential is 0.65 V. the local cell potentials can be as high as 0.76 V in the entry regions of the tube (i.e., left-hand regions of Fig. 4). The locally higher cell potentials cause locally lower current densities. To maintain comparable electric-potential variations within both electrodes, many more attachment points are needed on the cathode, which has higher electrical-resistance. In the downstream regions of the tube, where the current density is diminished, the local electric-potential variations are also diminished.

Figs. 5 and 6 show the model results for the reduced-attachment, where cathode attachment is reduced from 50 to 25 points. This also causes the bus resistance between attachment points to double. Compared to the base case, reducing the cathode attachment causes much higher electric-potential variations between attachment points in the bus and within the cathode. Further, the reduced-attachment causes much greater variations in local cell potential and current density. Overall the effective operating potential of the reduced-attachment cell is substantially higher than the terminal potential.

The local variations in current density are sufficient to cause noticeable variations in the MEA temperature (lower panel of Fig. 5). This is the result of locally varying heat generation within the MEA. As should be expected because of the convective nature of the flow, the temperature profiles within the gas flow are smooth.

Because the local cell potentials across the MEA are higher for the reduced-attachment case, the local current densities are lower. This, in turn, causes lower heat release and thus lower cell and flow temperatures. Compared to the base case, the fuel-consumption rate is lower in the upstream regions and greater in the downstream regions. Despite the local high-frequency variations, the overall more-uniform fuel consumption rates and cell temperatures could be viewed as having some benefits.

Fig. 7 shows the model results for the case without anode attachment. For anode-supported tubes with cathodes on the

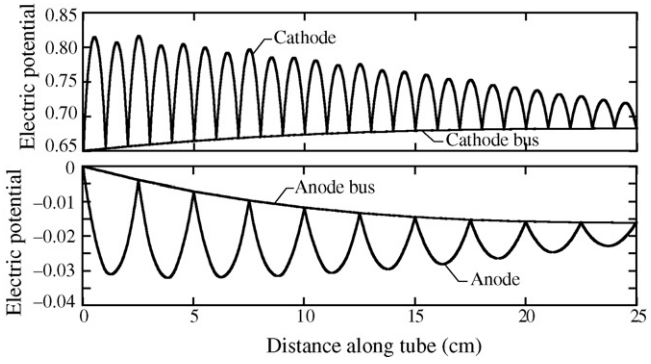

Fig. 6. Local electric-potential profiles for the reduced-attachment case.

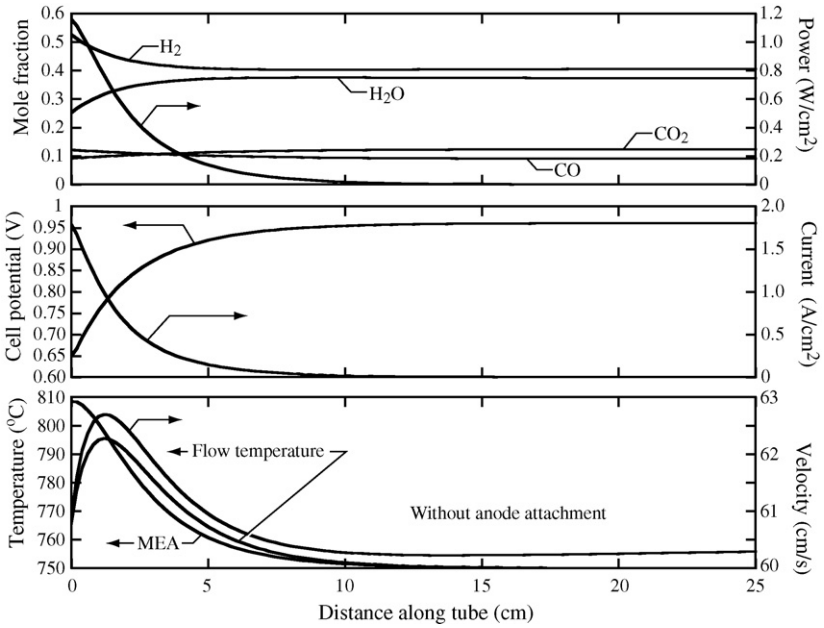

Fig. 7. Solution profiles without external anode current collection.

outside, providing cathode current collection is generally easier than anode current collection where attachments must be made inside the tube. Thus, it is interesting to understand the impact of eliminating the anode current collection. This example assumes perfect cathode current collection (i.e., uniform cathode electric potential along length of the tube). With anode current collection, all electric current must flow axially through the anode structure toward the terminal at the end. Therefore, the cell potential must increase along the tube length. For the parameters in this example, the cell voltage increases from the terminal potential of 0.65 V (at $x = 0$ cm.) to the open circuit potential of about 0.96 V within the first 10 cm of the tube. Once the open-circuit potential is reached no further fuel can be consumed, and thus no more current can be produced.

Eliminating anode current collection results in very poor performance for this example. The net power is low, and it is all produced within the first 10 cm of the tube. Fuel utilization is low, with only a small fraction of the H_2 consumed. Significant axial temperature gradients in the entry regions are also potentially problematic.

Fig. 8 shows solution profiles for the case of uniform cell potential at $E_{cell} = 0.65$ V. This is a limiting case, assuming perfect current collection on both the anode and cathode sides. Comparing Fig. 8 with Figs. 3 and 5, it is evident that the

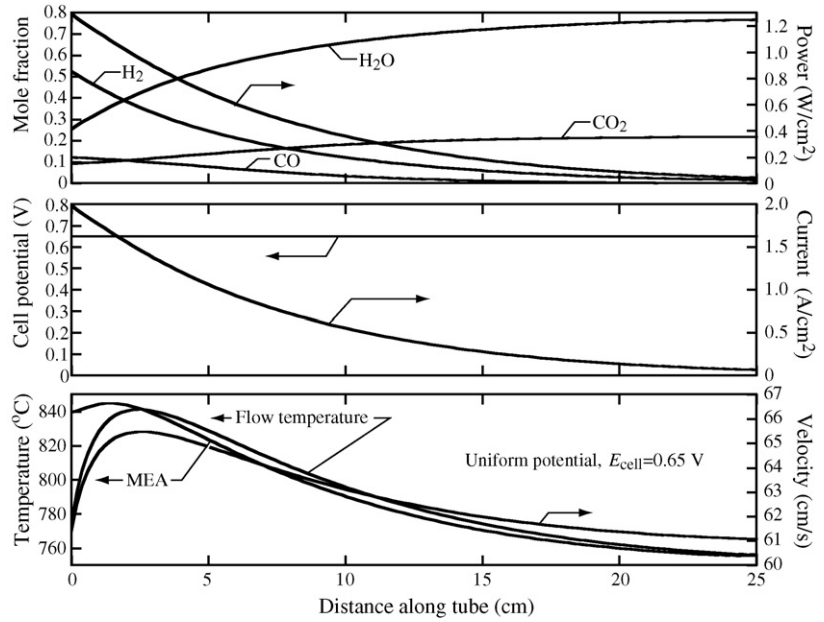

Fig. 8. Solution profiles at uniform cell potential of 0.65 V.

uniform-potential case is more similar to the base case than the reduced-attachment case.

It is interesting to note the tube-wall temperature variations in the vicinity of the tube inlet. The wall temperature at the inlet end is about 812 ° C for the base case, 790 ° C for the reduced-attachment case, 808 ° C for the without-anode-attachment case, and 840 ° C for the fixed-cell-potential case. These temperature variations, which are due to local heat release associated with chemical and electrochemical reactions within the anode and the ohmic losses across the MEA structure, are strongly coupled with the local current density. The local current density, in turn, is a strong function of the local temperature and the local cell potential. Therefore, it may be possible to design the current-collection system to control the cell-potential profile, seeking to achieve more uniform distributions of the current density and the temperature.

Overall cell performance can be measured in terms of conversion efficiency, fuel utilization, and power density [29]. The cell efficiency is defined as

$$\varepsilon = \frac{W_e}{Q_{in}} = \frac{\int i_e E_{cell}\, dA}{\dot{m}_{f,in}\Delta h_{f,in}} \tag{36}$$

where W_e is the electrical work output and Q_{in} is the heat that would be released upon full oxidation of the inlet fuel stream. The inlet fuel mass flow rate is $\dot{m}_{f,in}$ and $\Delta h_{f,in}$ is the specific enthalpy associated with completely oxidizing the fuel stream. The electrical work is the product of the current density i_e and operating voltage E_{cell}, integrated over the active membrane-electrode assembly (MEA) area. Fuel utilization U can be written as

$$U = 1 - \frac{\dot{m}_{f,out}\Delta h_{f,out}}{\dot{m}_{f,in}\Delta h_{f,in}} \tag{37}$$

where the "in" and "out" refer to the inlet and outlet of the fuel cell. The Δh refers to the specific enthalpy associated complete oxidation of any available fuels. This definition accounts for the energy content of any remaining fuels (or fuel byproducts) that leave in the fuel-cell exhaust. These definitions consider only performance within the SOFC, not overall system performance.

Table 3 compares the cell performance from all cases. Except the case without anode current collection, the overall efficiency and fuel utilization for the other cases are comparable. The uniform-cell-potential case shows about 5% lower cell efficiency than the cases with discrete current collection. Since a large amount of fuel can not be consumed for the case without anode current collection, fuel utilization and cell efficiency is dramatically lower.

Table 3
Predicted overall performance for alternative current collection

Case name	Efficiency (%)	Utilization (%)	Power (W)
Base case	52.5	95.3	32.4
Reduced cathode attachment	52.9	90.4	32.7
Without anode collection	14.6	24.1	9.0
Uniform cell potential	48.6	97.2	30.0

It is interesting to note that the efficiency and power density are slightly higher in the reduced-attachment case than in the base case. Efficiency and power density depend on operating potential, with efficiency usually maximum at operating potentials near 0.8 V [29]. The power density depends much more strongly on details of MEA performance, but usually peaks at lower operating potentials in the range of 0.6–0.7 V. The reduced-attachment case has a higher effective operating potential, which tends to increase efficiency. However, the reduced-attachment case has lower fuel utilization. Thus, it should be possible to increase its performance by reducing fuel flow rate. The uniform-cell-potential case shows lower efficiency than either of the discrete current-collection cases. This is primarily due to the low operating potential of 0.65 V. A uniform cell potential of around 0.8 V would lead to the highest efficiency.

6. Summary and conclusions

This paper develops and applies a computational model to assist current-collection design for tubular anode-supported solid-oxide fuel cells. The fuel cell model considers mass, momentum, and energy balances within the tube flow, reactive porous-media transport within the electrodes, electrochemical charge-transfer, and energy balances within the tube wall (i.e., the MEA). The current-collection electrical network considers multiple discrete attachment points to the cathode and anodes, as well as an axial bus that feeds current to the cell terminals.

The primary purpose of this paper is to document the modeling approach, not specifically optimize current collection for a particular cell. Nevertheless, even with a few examples, some interesting observations can be made. Cell performance depends on the current-collection design. The resistances and the attachment points can significantly affect local temperature and species profiles along the tube length, as well as overall performance measures like efficiency, fuel utilization, and power density. Predictive models can be a valuable guide in the design of tubular SOFC cells and the required current-collection strategy. Certainly increasing the number of current-collection points leads to more uniform cell potential along the length of the tube. Because of higher electrical-resistance within typical cathodes, more attachments points are usually needed on the cathode than on the anode. However, even in cases with attachment separations leading to as much as 150 mV variations in the local cell potential, overall performance measures such as efficiency and utilization are not strongly affected.

The nominal cell used for illustration in this paper has a relatively small inner tube diameter (8 mm) and is relatively long (25 cm). This cell can generate net power around 30 W. With an operating potential of around 0.7 V, the axial buses must carry over 40 Amps. For the conditions used as examples in this paper, an anode bus made of silver needs to be over 4 mm in diameter. Clearly a 4-mm-diameter wire within an 8-mm-diameter tube would significantly restrict flow area. The size and design of current collection, particularly inside anode tubes, can be a significant challenge in scaling to large tube dimensions.

Acknowledgements

This work was supported by the Office of Naval Research through a Research Tools Consortium grant number N00014-05-1-0339. Dr. Jerry Martin (Mesoscopic Devices, LLC) played an important role in motivating this study. We gratefully acknowledge many insightful discussions with Dr. Grover Coors (CoorsTek, Inc.) concerning electric-current distribution within tubular fuel cells.

References

[1] N.M. Sammes, Y. Du, R. Bove, J. Power Sources 145 (2005) 428–434.
[2] Y. Du, N.M. Sammes, J. Power Sources 136 (2004) 66–71.
[3] T.L. Nguyen, T. Honda, T. Kato, Y. Iimura, K. Kato, A. Negishi, K. Nozaki, M. Shiono, A. Kobayashi, K. Hosoda, Z. Cai, M. Dokiya, J. Electrochem. Soc. 151 (2004) A1230–A1235.
[4] J. Pusz, A. Mohammadi, N.M. Sammes, J. Fuel Cell Sci. Technol. 3 (2006) 482–486.
[5] S. Nagata, A. Momma, T. Kato, Y. Kasuga, J. Power Sources 101 (2001) 60–71.
[6] P. Aguiar, D. Chadwick, L. Kershenbaum, Chem. Eng. Sci. 57 (2002) 1665–1677.
[7] P. Aguiar, D. Chadwick, L. Kershenbaum, Chem. Eng. Sci. 59 (2004) 87–97.
[8] P.W. Li, M.K. Chyu, J. Electrochem. Soc. 124 (2003) 487–498.
[9] P.W. Li, K. Suzuki, J. Electrochem. Soc. 151 (2004) A548–A557.
[10] P.W. Li, L. Schaefer, M.K. Chyu, J. Heat Transfer 126 (2004) 219–229.
[11] P.W. Li, M.K. Chyu, J. Heat Transfer 127 (2005) 1344–1362.
[12] S. Campanari, P. Iora, J. Power Sources 132 (2004) 113–126.
[13] R. Suwanwarangkul, E. Croiset, M.D. Pritzker, M.W. Fowler, P.L. Douglas, E. Entchev, J. Power Sources 154 (2006) 74–85.
[14] R. Suwanwarangkul, E. Croiset, E. Entchev, S. Charojrochkul, M.D. Pritzker, M.W. Fowler, P.L. Douglas, S. Chewathanakup, H. Mahaudom, J. Power Sources 161 (2006) 308–322.
[15] T. Nishino, H. Iwai, K. Suzuki, J. Fuel Cell Sci. Technol. 3 (2006) 33–44.
[16] R.J. Boersma, N.M. Sammes, C.J. Fee, Solid State Ionics 135 (2000) 493–502.
[17] T. Suzuki, T. Yamaguchi, Y. Fujishiro, M. Awano, J. Power Sources 160 (2006) 73–77.
[18] T. Suzuki, T. Yamaguchi, Y. Fujishiro, M. Awano, J. Power Sources 163 (2007) 737–742.
[19] H. Zhu, R.J. Kee, V.M. Janardhanan, O. Deutschmann, D.G. Goodwin, J. Electrochem. Soc. 152 (2005) A2427–A2440.
[20] R.J. Kee, M.E. Coltrin, P. Glarborg, Chemically Reacting Flow: Theory and Practice, John Wiley, 2003.
[21] G.K. Gupta, E.S. Hecht, H. Zhu, A.M. Dean, R.J. Kee, J. Power Sources 156 (2006) 434–447.
[22] E.A. Mason, A.P. Malinauskas, Gas Transport in Porous Media: The Dusy-Gas Model, Elsevier, New York, 1983.
[23] E.S. Hecht, G.K. Gupta, H. Zhu, A.M. Dean, R.J. Kee, L. Maier, O. Deutschmann, Appl. Catal. A 295 (2005) 40–51.
[24] V. Grigull, H. Tratz, Int. J. Heat Mass Transfer 8 (1965) 669–678.
[25] G. Groppi, A. Belloli, E. Tronconi, P. Forzatti, Chem. Eng. Sci. 50 (1995) 2705–2715.
[26] P. Deuflhard, E. Hairer, J. Zugck, Num. Math. 51 (1987) 501–516.
[27] J.F. Grcar, R.J. Kee, M.D. Smooke, J.A. Miller, One-Dimensional Premixed Flames. Proc. Combust. Inst. 21 (1986) 1773–1782.
[28] J.R. Ferguson, J.M. Fiard, R. Herbin, J. Power Sources 58 (1996) 109–122.
[29] H. Zhu, R.J. Kee, J. Power Sources 161 (2006) 957–964.